Article

Facile Synthesis of Oxygen-Doped g-C_3N_4 Mesoporous Nanosheets for Significant Enhancement of Photocatalytic Hydrogen Evolution Performance

Tiekun Jia *, Jingjing Li, Zhao Deng, Dongsheng Yu, Joong Hee Lee

Posted Date: 16 January 2024

doi: 10.20944/preprints202401.1170.v1

Keywords: O-doped; g-C3N4; Nanosheets; Porous structure; Hydrogen evolution doi:10.20944/preprints202401.1170.v1

Article

Facile Synthesis of Oxygen-Doped g-C_3N_4 Mesoporous Nanosheets for Significant Enhancement of Photocatalytic Hydrogen Evolution Performance

Tiekun Jia [1,*], Jingjing Li [1,*], Zhao Deng [2], Dongsheng Yu [1] and Joong Hee Lee [3]

[1] School of Materials Science and Engineering &Henan Province International Joint Laboratory of Materials for Solar Energy Conversion and Lithium Sodium based Battery, Luoyang Institute of Science and Technology, Luoyang, 471023, P. R. China; tiekunjia@126.com; lijj2023@lit.edu.cn; yudongsheng@lit.edu.cn
[2] State Key Lab of Materials Synthesis and Processing, Wuhan University of Technology, Wuhan, 430070, P. R. China; dengzhao@whut.edu.cn
[3] Department of Nano Convergence Engineering, Jeonbuk National University, Jeonju 54896, Korea; jhl@jbnu.ac.kr
* Correspondence: tiekunjia@126.com or tiekun_jia@lit.edu.cn (T. J.)

Abstract: In this work, oxygen-doped g-C_3N_4 mesoporous nanosheets (O-CNS) were synthesized via a facile recrystallization method with the assistance of H_2O_2. The crystal phase, chemical composition, morphological structure, optical property, electronic structure and electrochemical property of the prepared O-CNS samples were well investigated. The morphological observation combining with nitrogen adsorption-desorption results demonstrated that the prepared O-CNS samples possessed nanosheets-like morphology with porous structure. The O doping into g-C_3N_4 resulted in the augment of specific surface area, which could provide more active sites for photocatalytic reaction. Simultaneously, the visible-light absorption capacity of O-CNS samples was boosted owing to the regulation of O doping. The built energy level induced by the O doping could accelerate the migration rate of photoinduced carriers, and the porous structure was most likely to speed up the release of hydrogen during photocatalyic hydrogen process. Resultantly, the photocatalytic hydrogen production rate of the optimized oxygen-doped g-C_3N_4 nanosheets reached up to 2012.9 $\mu mol \cdot h^{-1} \cdot g^{-1}$, which was 13.4 times higher than that of bulk g-C_3N_4. Thus, the significantly improved photocatalytic behavior was imputed to the porous structure, the augment of active sites, and the enhancement of visible light absorption and charge separation efficiency.

Keywords: O-doped; g-C_3N_4; nanosheets; porous structure; hydrogen evolution

1. Introduction

Photocatalytic hydrogen production is an advanced technology that converts renewable solar energy into clean hydrogen energy. As for this advanced technology, photocatalyst is a pivotal factor affecting the efficiency of photocatalytic hydrogen evolution. Thus, it is crucial to develop an efficient, stable and low-cost photocatalyst for facilitating the rapid development of photocatalytic hydrogen evolution [1]. Graphitic carbon nitride (g-C_3N_4) is a new type of organic semiconductors with the band gap of about 2.7 eV, which is reckoned as a promising photocatalytic material due to its nontoxicity, element abundance, suitable bandgap structure, stable physicochemical properties and good photoelectrochemical performance [2–4]. However, single component g-C_3N_4 still has some inherent defects, for instance, small specific surface area, limited solar light utilization, and long transfer distance of photogenerated charge [5,6], which seriously limit its potential application in photocatalytic hydrogen production.

By now, researchers have explored some effective modification methods to address the aforementioned shortcomings and improve the photocatalytic hydrogen production behavior of g-

C_3N_4, such as element doping [7], morphology modulation [8], noble metal deposition [9] and composites with other materials [10–12]. Amongst these modification methods, element doping has been extensively accepted and adopted to improve cata-lytic activity due to its easy operation and simple control. As is well known, the atomic radius and physicochemical properties of O element are similar to those of C and N elements, thus it is an intriguing and challenge research to adopt oxygen doping for modifying g-C_3N_4 with enhanced photocatalytic hydrogen evolution performance. In previous studies, Shi ʻgroup [13] conducted an investigation on the thermal gas shocking synthesis and photocatalytic performance of 2D ultrathin oxygen doped g-C_3N_4 photocatalysts, and found that the electronic structure of oxygen-doped g-C_3N_4 photocatalysts was optimized and the carrier separation rate was significantly elevated. Jia and his coworkers [14] prepared S and O co-doped g-C_3N_4 nanosheets through a two-step annealing process with melamine as the g-C_3N_4 precursor for efficient hydrogen generation. Tang' group [15] developed a defect-engineering approach to prepared O dopant and N defect in g-C_3N_4 framework. Saka and his coworkers [16] prepared oxygen-doped g-C_3N_4 through a pyrolysis route combining with the treatment of HNO_3 solution. All these achievements on oxygen-doped g-C_3N_4 are deeply impressive; however, it is especially desirable to explore an in situ and green strategy for achieving oxygen-doped g-C_3N_4 with improved photocatalytic hydrogen evolution behavior.

In this work, oxygen-doped g-C_3N_4 porous nanosheets with large specific surface area were synthesized via a simple recrystallization method with H_2O_2 as the dopant source. The structure, morphology, chemical composition, optical absorption, specific surface area and carrier separation of the photocatalysts were comprehensively characterized. The photocatalytic activity and stability of the photocatalysts were evaluated by hydrogen production under the visible light illumination. In addition, the possible mechanism of the enhanced photocatalytic hydrogen evolution performance was proposed in this work. Up to now, there are limited reports on the investigation of photocatalytic hydrogen production over oxygen-doped g-C_3N_4 porous nanosheets.

2. Materials and Methods

2.1. Materials

All the starting materials, containing urea ($(NH_2)_2CO$), hydrogen peroxide solution (H_2O_2), chloroplatinic acid (H_2PtCl_6), triethanolamine (TEOA), and sodium sulfate (Na_2SO_4) were of analytical grade, and directly used without further purification.

2.2. Preparation of g-C_3N_4 (u-CNB) and O-doped g-C_3N_4 (O-CNS) samples

2.2.1. Preparation of g-C_3N_4 (u-CNB)

The bulk g-C_3N_4 photocatalyst was prepared by thermal condensation polymerization. 10 g of urea was placed in the semi-closed corundum crucible and calcined in a muffle furnace at 550 °C for 2 h with the rate of 2 $°C\cdot min^{-1}$. After being spontaneously cooled to ambient temperature, the obtained light yellow product was taken out, and fully ground into powder for further use.

2.2.2. Preparation of O-doped g-C_3N_4 (O-CNS)

In a typical process, 10 g of $(NH_2)_2CO$ was completely dissolved in different volumes of commercial H_2O_2 (30 vol%) solution under ultrasound, and then dried at 80 °C for 15 h to recrystallize $(NH_2)_2CO$. Subsequently, the recrystallized $(NH_2)_2CO$ was placed in a quartz tube and heated at 550 °C for 2 h with the rate of 2 $°C\cdot min^{-1}$ under Ar environment. Finally, the calcined products were ground and collected, and alternately washed with dilute nitric acid solution ($1 mol\cdot L^{-1}$), deionized water and ethanol to obtained O-CNS samples. The volumes of H_2O_2 solution were 57.5 mL, 60 mL, 62.5 mL, 65 mL, 67.5 mL and 70 mL, so, the obtained O-CNS samples were respectively expressed as 57.5 O-CNS, 60 O-CNS, 62.5 O-CNS, 65 O-CNS, 67.5 O-CNS and 70 O-CNS, correspondingly.

doi:10.20944/preprints202401.1170.v1

2.3. Characterization

The X-ray diffraction (XRD) patterns of the as-prepared photocatalysts were conducted on a Bruker D8 advance diffractometer with Cu Ka radiation. X-ray photoelectron spectroscopy (XPS) was recorded on an ESCALAB 250 Xi spectrometer. The scanning electron microscopy (SEM) observation was performed on a Hitachi S-4800 electron microscope with the accelerating voltage of 5 kV. Transmission electron microscopy (TEM) and scanning transmission electron microscopy (STEM) were conducted to investigate the porous structure of the obtained O-CNS sample on a FEI Talos F200S transmission electron microscope with the voltage of 200 kV. Brunauer-Emmett-Teller (BET) specific surface areas were recorded on a Tristar II 3020 surface area analyzer. UV-visible diffuse reflectance spectra (DRS) were collected on a TU-1901 UV-Vis spectrometer. Electron paramagnetic resonance (EPR) spectra were measured on a Bruker MEX-nano spectrometer.

2.4. Photoelectrochemical measurements

The photoelectrochemical properties of the obtained samples were tested in Na_2SO_4 electrolyte solution (0.5M, pH=6.8) through a three-electrode system, which is equipped with a counter electrode (Pt sheet), a reference electrode (Ag/AgCl solution), and a working electrode (FTO conductive glass with spin coated photocatalysts) [17]. A Xenon lamp (300W) equipped with a 420 nm cut-off quartz optical filter was taken as the visible light source in the photoelectrochemical measurements. The details for the measurements were already reported in our previous work [18].

2.5. Photocatalytic hydrogen evolution experiments

Photocatalytic hydrogen production experiments were conducted in a closed glass gas circulation system (Labsolar III AG), which was connected to an Agilent 7890B gas chromatograph for online testing. A PLS-SXE-300W xenon lamp with a 420 nm cutoff filter was used as the visible light source. The vertical distance from the xenon lamp light to the surface of the mixed solution is 10 cm and the inner diameter of the reactor is 8 cm. 50 mg of photocatalyst was uniformly dispersed in the 100 mL aqueous solution containing 20% triethanolamine (TEOA) and H_2PtCl_6 solution (1wt%), which was respectively used as sacrificial agent and co-catalyst. Every half hour, the xenon light source was turned on and the amount of hydrogen generation was detected for one time.

3. Results

3.1. Structure and morphology

The effect of the amount of H_2O_2 on the crystal structure of the as-obtained samples was analyzed by XRD and the results are shown in Figure 1. It can be seen that the u-CNB sample exhibited two clear and sharp diffraction peaks near 13.2° and 27.8°, corresponding to the (100) and (002) crystal planes of the g-C_3N_4, respectively [19,20]. However, after incorparating O atoms into g-C_3N_4 crystal, the diffraction peaks at 13.2° for all O-CNS samples disappeared. Besides above, the diffraction peak around 27.8° of O-CNS samples became wider and weaker than that of u-CNB, and the intensity gradually decreased with the increase of H_2O_2 content, suggesting that the introduction of O atoms affected the structure of g-C_3N_4 crystals.

As is presented in Figure 2, the elemental composition and chemical status of the synthesized samples were characterized by XPS. From the survey spectra (Figure 2a), three stong signals for C, N, and O element appeared for the 65 O-CNS sample, indicating the exsistence of O element. The weak signal of O 1s in u-CNB was mainly originated from adsorbed oxygen in the XPS measurement. Interestingly, the intensity of the C 1s and N 1s peaks in the 65 O-CNS sample was weaker than those in u-CNB, presumably due to the doping of O element. Figure 2b-d show the high-resolution XPS spectra. Two dominant peaks for C 1s was situated around 284.6 and 288 eV (Figure 2b), and the high-resolution spectrum of N 1s could be deconvoluted into four smaller peaks with binding energy of 398, 399.6, 400.8 and 404.2 eV (Figure 2c). Figure 2d displays the high-resolution spectrum of O 1s of the 65 O-CNS sample, in which the peak at 531.8 eV was ascribed to the formation of N-C-O material [21–23]. Summarily, the results mentioned above provided a strong proof for the presence and chemical status of O ions in the 65 O-CNS sample. Additionally, vacancy defects could be correspondingly formed to compensate for the valence difference of N ions and O ions.

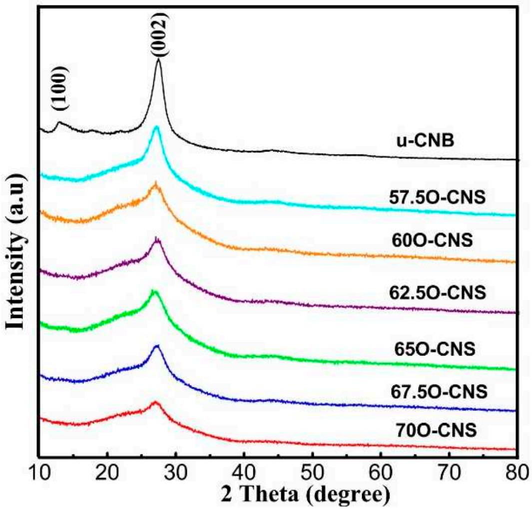

Figure 1. XRD patters of u-CNB and O-CNS samples.

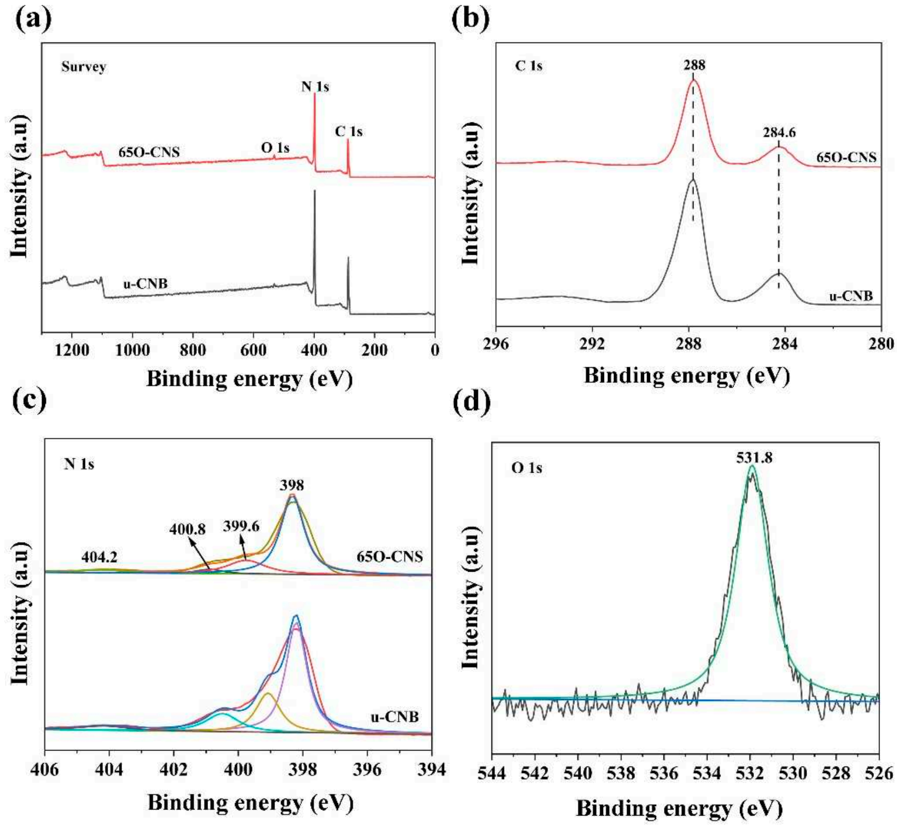

Figure 2. (a) Survey spectra, (b) C 1s spectra, and (c) N 1s spectra of u-CNB and 65 O-CNS, (d) O 1s spectra of 65 O-CNS.

Figure 3 shows the SEM images of u-CNB and 65 O-CNS samples. From Figure 3a, the u-CNB sample possessed a block-like structure assembly with stacking layers. That is to say, the u-CNB sample obtained by direct calcination exhibited irregularly block morphology, which was perhaps insufficient for providing abundant active sites for photocatalytic hydrogen production performance. Contrarily, a typical curled nanosheet-like structure appeared for the 65 O-CNS sample, as is seen in Figure 3b. Thereby, it is reasonably inferred that the addition of H_2O_2 was mostly likely to play a great role in tuning the morphological structure. The feature of such morphological structure would endow the 65 O-CNS sample with larger specific surface area, which further was benefical for augmenting active sites of the hydrogen production reaction.

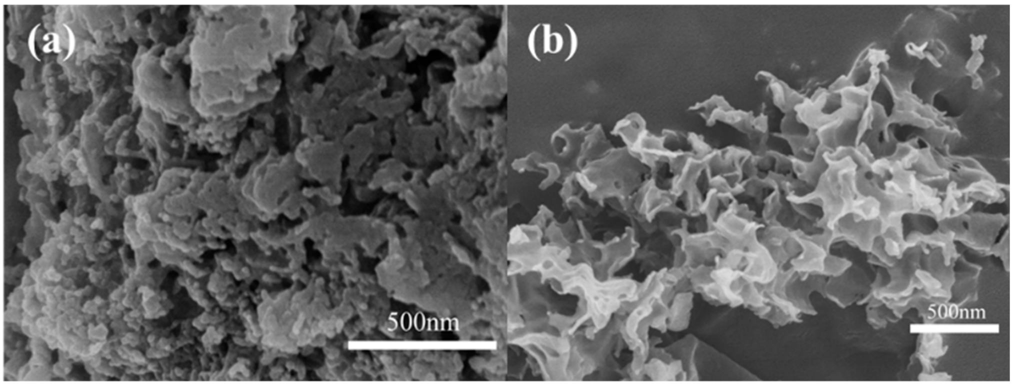

Figure 3. SEM images of (a) u-CNB and (b) 65 O-CNS.

The morphological structure of the 65 O-CNS photocatalyst was further examined by TEM and STEM images. As is observed from Figure 4a, the 65 O-CNS sample consists of a mass of nanosheets with a relatively thin thickness of approximately 10 nm. Furthermore, it is clear from the magnified image (Figure 4b) that some irregular pores were distributed throughout thin nanosheets, resulting in the formation of porous structure, which was beneficial for acquiring large specific surface area. The formation of porous structure was presumably associated with the bubbles produced during the polycondensation process with the assistance of H_2O_2. Therefore, it could be drawn a conclusion that the introduction of H_2O_2 indeed regulated the morphological structure. The element distribution of 65 O-CNS was revealed by high angle annular dark-field (HAADF) and energy dispersive X-ray spectroscopy (EDS) elements mapping, as illustrated in Figure 4c-f. It is clear from Figure 4c-f that C, N and O elements were uniformly distributed throughout the 65 O-CNS sample, which further confirmed the presence of O element in the 65 O-CNS sample. As for Cu element, it came from copper mesh in the sample preparation. Based on the above analysis, the oxygen-doped C_3N_4 thin nanosheets with porous structure were successfully prepared with H_2O_2 as the dopant source.

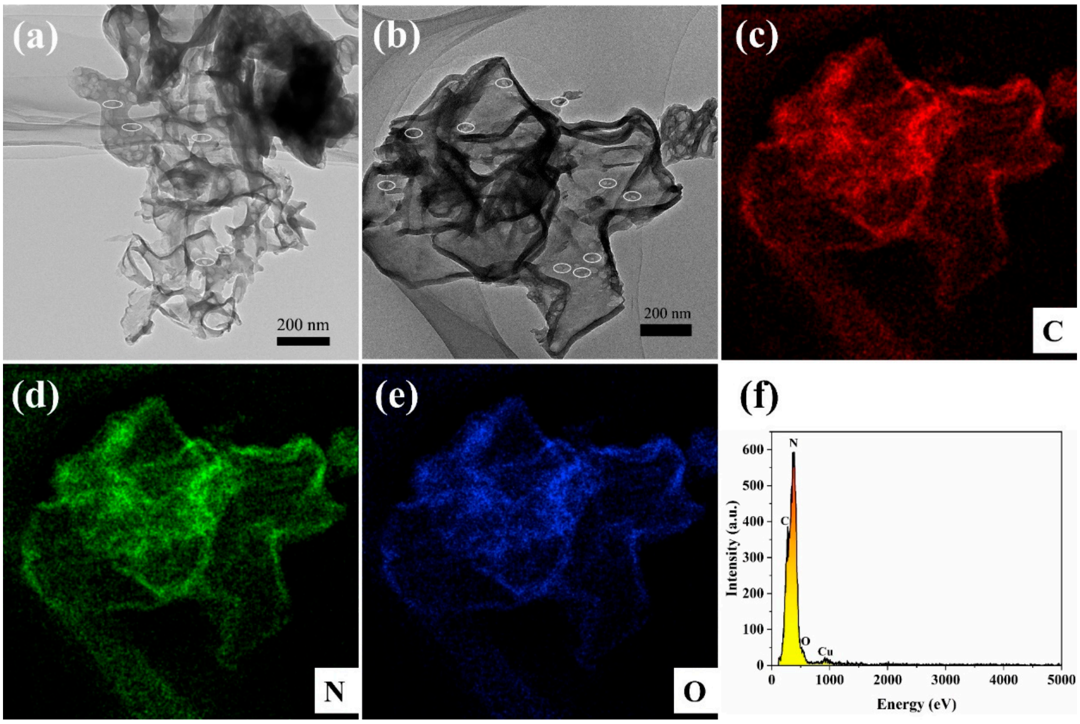

Figure 4. (a) TEM image, (b) HAADF-STEM image, (c, d, e) elemental mapping images of C, N, and O elements, (f) energy diffraction spectrum of 65 O-CNS.

3.2. Specific surface area and optical properties

Figure 5 shows the N_2 adsorption-desorption isotherms of u-CNB and different O-doped C_3N_4 samples. Obviously, the N_2 adsorption-desorption isotherm for O-doped C_3N_4 samples with higher N_2 volume adsorbed at P/P_0 were classified as type IV isotherms with H_3 hysteresis loops, manifesting the mesoporous nature of the resulting samples. However, for u-CNB sample, a lower volume N_2 adsorbed at high P/P_0 was perhaps ascribed to the severe agglomeration of block-like particles [24]. Table 1 shows the specific surface area and pore size distribution of u-CNB and different O-doped C_3N_4 samples. Among them, u-CNB had the smallest specific surface area, attributable to the blocky structure formed by severe stacking of layers, while 65 O-CNS sample possessed the largest specific surface area due to the nanosheets stacking. The augment of specific surface area for the 65 O-CNS sample was most likely to increase the active sites for catalytic reaction, which would facilitate the significant improvement of photocatalytic hydrogen production performance.

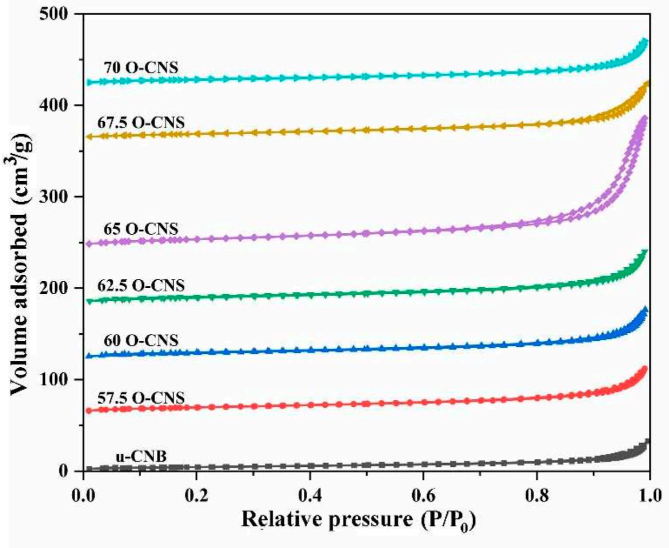

Figure 5. N_2 adsorption-desorption isotherms of the as-obtained samples.

Table 1. The specific surface area and pore size distribution value of the samples.

Samples	BET ($m^2 \cdot g^{-1}$)	Average pore Width (nm)	Pore volume ($cm^3 \cdot g^{-1}$)
u-CNB	13.9	9.125	0.0567
57.5 O-CNS	33.8	27.256	0.327
60 O-CNS	32.4	34.321	0.465
62.5 O-CNS	34.5	40.539	0.544
65 O-CNS	48.2	43.246	0.583
67.5 O-CNS	31.3	46.784	0.614
70 O-CNS	28.8	49.653	0.638

As is well known, the light absorption capacity has a notable effect on the photocatalytic hydrogen production performance. To compare the difference of the light absorption capacity between u-CBN and 65 O-CNS sample, the UV-Vis diffuse reflection (DRS) spectra of u-CNB and 65 O-CNS samples was conducted, and the results are shown in Figure 6a. Quite evidently, the intensity of light absorption for the 65 O-CNS sample was significantly strengthened from ultraviolet to visible light region in comparison with that of u-CBN. Besides above, as compared with u-CNB, the absorption edge of 65 O-CNS sample was redshifted, indicating the visible light absorption range was broadened due to the incorporation of the doping. By extrapolating the linear portion of the Tauc plots (Figure 6b), the bandgap energy (Eg) of u-CNB was determined to be approximately 2.62 eV, while the Eg of 65 O-CNS decreased to about 2.5 eV, indicating that the introduction of O atoms could regulate the electronic structure and enhance the light capture ability [25–27]. Thus, the improvement of visible-light absorption capacity was likely to provide probability for producing more photo-generated carriers, and further improve its catalytic performance.

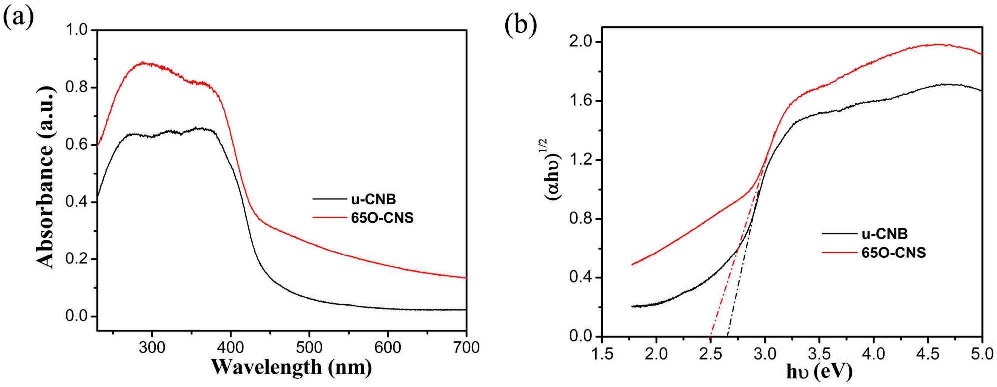

Figure 6. (a) UV-Vis DRS spectra and (b) the plot of $(\alpha h\nu)^{1/2}$ vs photon energy (hv) for bandgap energies of u-CNB and 65 O-CNS.

3.3. Electron paramagnetic resonance and electrochemical measurements

The unpaired electrons of the prepared u-CNB and 65 O-CNS samples were tested by electron paramagnetic resonance (EPR) at ambient temperature and the result is shown in Figure 7. In the magnetic field from 333 to 353 mT, the u-CNB and 65 O-CNS samples had only one Lorentz curve centered around a g value of 2.0034, which was considered as lone pair electrons in sp^2 hybrid carbon in g-C_3N_4 [28]. Moreover, the EPR signal intensity of the 65 O-CNS sample was much higher than that of u-CNB, suggesting that more unpaired electrons in 65 O-CNS sample were generated under illumination. The result of EPR also revealed that the recombination of photo-generated electron-hole pairs for the 65 O-CNS sample was substantially inhibited, compared with that of u-CBN.

As previous research work domonstated [25], the photocurrent response of semiconducting photocatalysts is capable of reflecting the transfer and separation of photoexcited electrons and holes. The migration rate of photo-generated electron-hole pairs in u-CNB and 65 O-CNS samples were further analyzed through electrochemical measurement. As is presented in Figure 8a, rapid and reversible photocurrent response sprouted for u-CNB and 65 O-CNS samples, indicating the stability and reproducibility. The photocurrent density of the 65 O-CNS sample was much larger than that of u-CNB, signifying that the migration rate of photogenerated carriers of the 65 O-CNS sample was much higher than that of u-CNB, demonstrating the remarkable elevation of the separaton and migration rate of photoexcited carriers. Figure 8b presents the Nyquist plots of electrochemical impedance spectra (EIS) for u-CNB and 65 O-CNS samples. According to previously reported work [29–31], the smaller the radius of the curve, the smaller the internal resistance. As expected, the impedance of the 65 O-CNS sample was smaller than that of u-CBN, revealing that more excited carriers could successfully migrate to the interface due to the restriction of carrier recombination. This result of EIS was also in good accordance with the results of photocurrent analysis. Based above, we can draw a conclusion that the migration rate of photogenerated carriers of the 65 O-CNS sample were remarkably accelerated and the recombination rate of photogenerated electron-hole pairs decreased significantly due to the O doping.

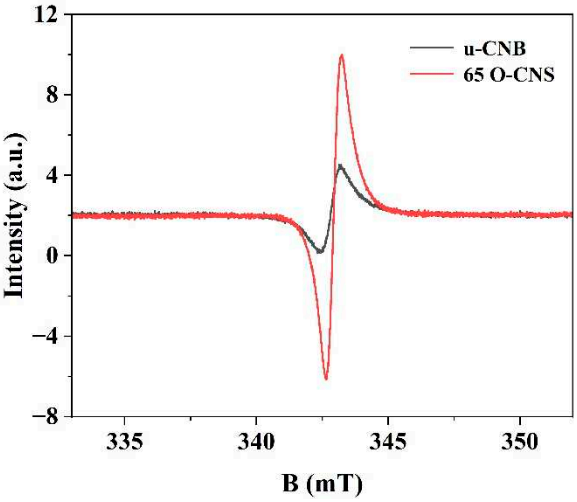

Figure 7. EPR spectra of u-CNB and 65 O-CNS.

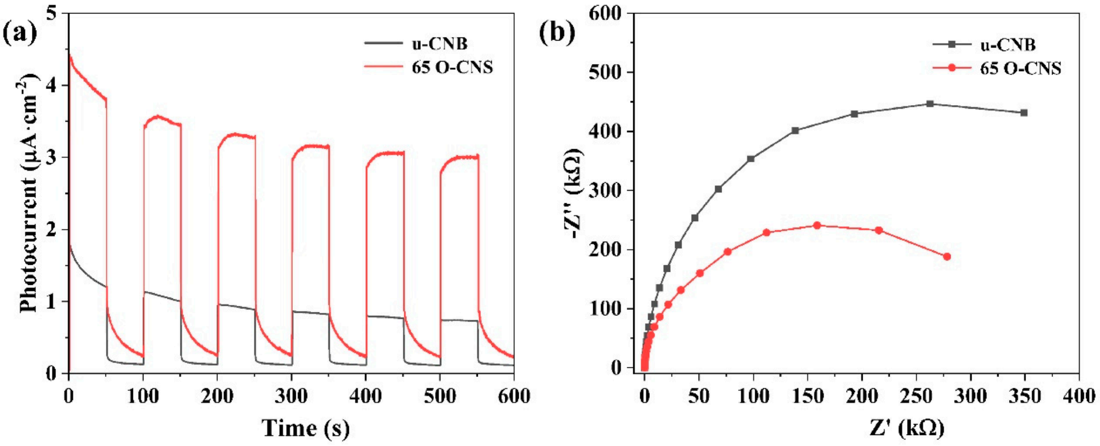

Figure 8. (a) Photocurrent curves and (b) electrochemical impedance spectra of u-CNB and 65 O-CNS electrodes.

3.3. Photocatalytic hydrogen production performance

The photocatalytic performance of different O-doped samples was evaluated by splitting water into hydrogen under visible light irradiation, and the results are shown in Figure 9. It can be seen from Figure 9a that the u-CNB sample had a very poor photocatalytic hydrogen production activity with a hydrogen production rate of 149.9 μmol·h^{-1}·g^{-1}. Satisfactorily, the hydrogen production performance of O-CNS samples was greatly improved with the increase of H_2O_2 amount. When the amount of H_2O_2 reached 65 mL, the obtained sample had the optimal hydrogen production rate of 2012.9 μmol·h^{-1}·g^{-1}, which was 13.4 times than that of u-CNB. With further increasing the amount of H_2O_2, the hydrogen production rate of the obtained samples did not increase constantly, but gradually decreased (Figure 9b). The reason for this trend can be summarized as follows. Firstly, the destruction of pore structures induced by excess H_2O_2 probably made an important contribution to the decrease of hydrogen evolution rate,which could also be evidenced by the decrease of surface area (Figure 5) with the increase of H_2O_2 volumes from 65mL to 70mL [32]. Secondly, the excess of H_2O_2 could result in the formation of more defects, which would act as recombination centers, leading to the increase of the recombination rate of photoinduced e$^-$-h$^+$ pairs. Accordingly, the hydrogen production rate of O doped CNS photocatalysts decreased when the loading amount of H_2O_2 exceeded the critical value of 65 mL. More importantly, the hydrogen production rate of the O-doped g-C_3N_4 was higher than that of most metal-free g-C_3N_4 photocatalysts under similar conditions (Table 2) [13,33–37]. In addition, the cycling experiments over the 65 O-CNS sample were conducted. As is found from Figure 9c, the photocatalytic hydrogen production rate of the 65 O-CNS sample exhibited a slight decline after three cycle tests. Additionally, the XRD pattern in Figure 9d showed that the crystal structure of 65 O-CNS exhibited no obvious change after cyclic experiments of photocatalytic hydrogen production. The above results indicated that the 65 O-CNS sample was of high stability as a photocatalyst for photocatalytic hydrogen production.

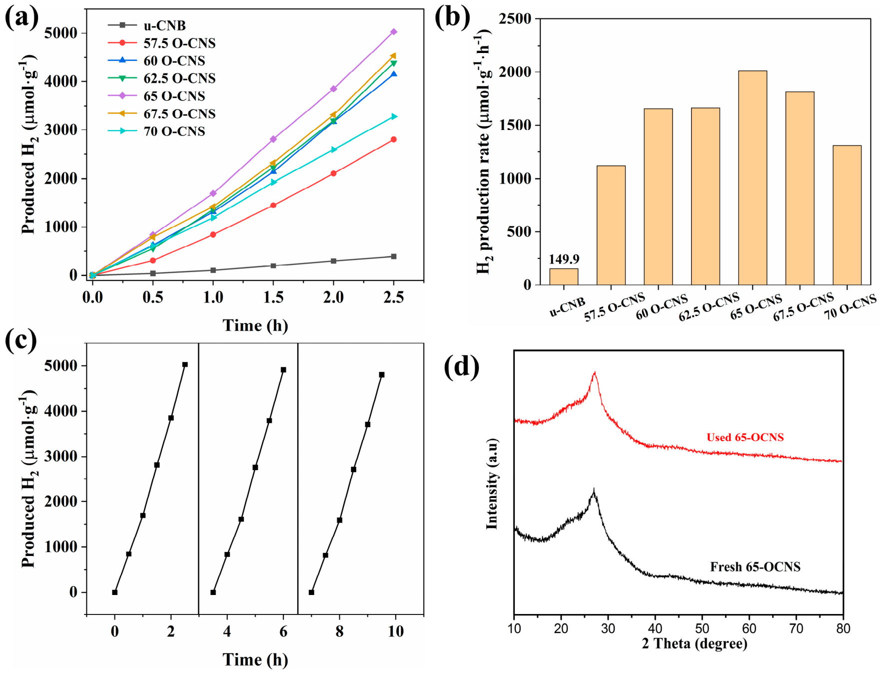

Figure 9. (a) Photocatalytic hydrogen production curves, (b) hydrogen production rate for u-CNB and O-CNS, (c) photocatalytic durability of 65 O-CNS and (d) XRD pattern of 65 O-CNS after cyclic runs.

Table 2. Comparison of hydrogen evolution of element-doped g-C_3N_4 photocatalysts.

Samples	Light source	Reactant solution	Hydrogen evolution ($\mu mol\ h^{-1}\ g^{-1}$)	Reference
O-doped g-C_3N_4 nanosheets	300W Xe Lamp (λ > 420 nm)	80 mL water+20 mL TEOA, 1% H_2PtCl_6	2012.9	This work
Pt/g-C_3N_4 nanotube	300W Xe Lamp (λ > 420 nm)	TEOA aqueous solution (100 mL, 10 vol%)	5304	Ref [33]
S-doped g-C_3N_4	300W Xe Lamp (λ > 420 nm)	50 mL aqueous TEOA solutions (10 vol%), 2% Pt	161.32	Ref [34]
Oxygen-doped g-C_3N_4 sheets	300 W Xenon lamp (λ > 420 nm)	100 mL aqueous solution containing 10 vol% TEOA, 3% Pt	2200	Ref [15]
N-Defective and S-Doped g-C_3N_4	300 W Xe lamp (λ > 420 nm)	10 mL TEOA+ 90 mL deionized water, 3% Pt	5651.5	Ref [35]
Carbon defective g-C_3N_4	300 W Xe lamp (λ > 420 nm)	100 mL of 10 vol% TEOA aqueous solution, 1% Pt	1534	Ref [36]
K-doped g-C_3N_4	300 W Xe lamp (λ > 400 nm)	100 mL containing 10 vol % TEOA, 3% Pt	1337.2	Ref [37]

3.4. Photocatalytic mechanism

In order to further investigate the enhancement mechanism of photocatalytic activity of oxygen-doped C_3N_4, the Mott-Schottky (M-S) plots of u-CNB and 65 O-CNS samples were depicted in Figure 10. The M-S plots of u-CNB and 65 O-CNS exhibited positive slopes, indicating the typical characteristics of n-type semiconductors. By intercepting on the horizontal axis in the M-S plots, the flat potentials of u-CNB and 65 O-CNS were calculated to be -0.58 eV and -0.69 eV (vs. NHE), respectively. The 65 O-CNS sample showed a more negative flat band potential than u-CNB, indicating a larger amount of electron accumulation and faster separation rate of photo-generated carriers in the 65 O-CNS photocatalyst. For n-type semiconductor, the potential of flat band is about 0.2 eV more positive than that of conduction band (CB) [38]. Therefore, the conduction band of u-CNB and 65 O-CNS was estimated to be -0.78 eV and -0.89 eV (vs. NHE), respectively. Combining with the UV-vis DRS results above, the valence band (VB) of the u-CNB and 65 O-CNS sample were calculated to be 1.84 eV and 1.61 eV(vs. NHE), respectively. On the basis of above demonstration, a proposed mechanism for the enhancement of photocatalytic behavior is schematically portrayed in Figure 11. Upon the exposure to visible light irradiation, the electrons (e^-) in O-CNS are excited, and migrate from the VB to CB, leaving holes in the VB (h^+). Then, the excited electrons will transfer from the CB of O-CNS to the surface of Pt particles. The accumulating electrons on the surface of Pt particles combine with hydrogen ions to produce H_2. At the same time, TEOA is oxidized to form $TEOA^+$ by photogenerated holes duiring the oxidation reaction process. The possible reaction equations involved in photocatalytic hydrogen evolution are as follows.

$$\text{O-CNS} + hv \rightarrow h^+ + e^- \tag{1}$$

$$H_2O + h^+ \rightarrow H^+ + \cdot OH \tag{2}$$

$$\text{TEOA} + h^+ \rightarrow \text{TEOA}^+ \tag{3}$$

$$e^- + H^+ \rightarrow H_2 \tag{4}$$

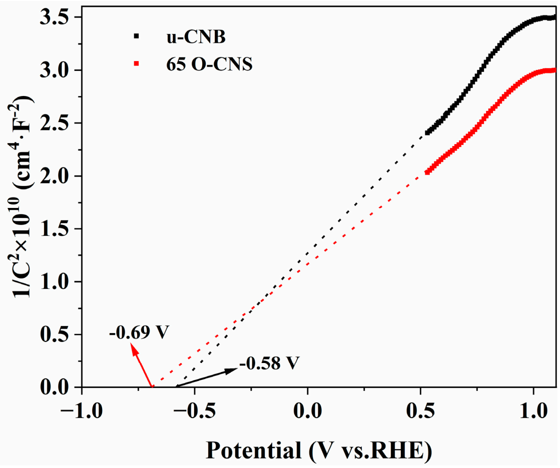

Figure 10. Mott-Schottky plots of u-CNB and 65 O-CNS.

Summarily, the O doping induced the formation of porous structure, the decrease of band gap, the regulation of energy level, and the improvement of the separation and migration rate of photogenerated carriers. The porous structure could presumably speed up the release of hydrogen during photocatalyic hydrogen process. The regulation of energy band endowed O-CNS with higher reduction capacity. The built energy levels formed by vacancy defects facilitated the efficient separation and transfer of photoexcited electrons. Therefore, the 65 O-CNS sample exhibited highest photocatalytic hydrogen production rate due to the synergistic effect of the improved visible light absorption capacity, the augmented active sites, and the enhanced photogenerated carrier separation rate.

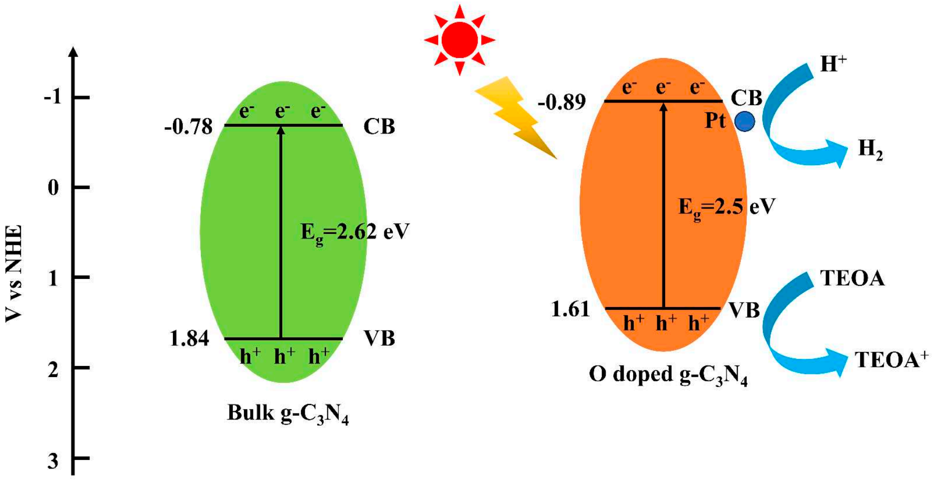

Figure 11. The mechanism of the photocatalytic hydrogen production of u-CNB and O-CNS under visible light irradiation.

5. Conclusions

In the present work, oxygen-doped g-C_3N_4 porous nanosheets were achieved through an in situ, easily controllable and environmentally friendly approach, using H_2O_2 as oxygen source. The modification of oxygen doping resulted in the formation of porous structure, vacancy defects and boosted visble-light absorption capacity. The vacancy defects shaped into novel energy level, which effectively restricted the recombination of photoinduced carriers. Simultaneously, the amount of O doping in g-C_3N_4 significantly affected the photocatalytic hydrogen evolution performance. Benefiting from the optimum amount of H_2O_2, the 65 O-CNS sample possessed the highest photocatalytic hydrogen production performance. The notable improvement of photocatalytic hydrogen evolution performance over the 65 O-CNS sample was mainly attributed to the porous structure, the increase of active sites, the boosted visible-light absorption capacity and the enhancement of photogenerated charge carriers' separation efficiency. This work will provide a new pathway for pursuing novel strategy for the preparation of element doped C_3N_4 photocatalysts with exceptional photocatalytic hydrogen evolution performance.

Author Contributions: Tiekun Jia conceived and designed the experiments; Zhao Deng carried out the synthetic experiment and photo-catalytic performance of the as-prepared samples; Jingjing Li measured the as-prepared samples; Tiekun Jia wrote the paper; Dongsheng Yu analyzed the data; Joong Hee Lee provided precise instruction.

Acknowledgments: The authors express grateful thanks to and the Department of Science and Technology of Henan Province, China (Henan Science and Technology Research Program, 222102520005 and 232102521021), and the Education Department of Henan Province for the fund support (21A430026).

Conflicts of Interest: The authors declare no conflict of interest.

References

1. Takata, T.; Jiang, J.; Sakata, Y.; Nakabayashi, M.; Shibata, N.; Nandal, V.; Domen, K. Photocatalytic water splitting with a quantum efficiency of almost unity. *Nature,* 2020, 581 (7809), 411-414.
2. Wu, M.; Zhang, J.; He, B.B.; Wang, H.W.; Wang, R.; Gong, Y.S. In-situ construction of coral-like porous P-doped g-C_3N_4 tubes with hybrid 1D/2D architecture and high efficient photocatalytic hydrogen evolution. *Appl. Catal. B: Environ.* 2019, 241, 159-166.

3. Liang, Q.; Zhang, C.J.; Xu, S.; Zhou, M.; Zhou, Y.T.; Li, Z.Y. In situ growth of CdS quantum dots on phosphorus-doped carbon nitride hollow tubes as active 0D/1D heterostructures for photocatalytic hydrogen evolution. *J. Colloid Interf. Sci.* 2020, 577, 1-11.
4. Jiang, L.B.; Yuan, X.Z.; Zeng, G.M.; Chen, X.H.; Wu, Z.; Liang, J.; Zhang, J.; Wang, H.; Wang, H. Phosphorus-and sulfur-codoped g-C_3N_4: facile preparation, mechanism insight, and application as efficient photocatalyst for tetracycline and methyl orange degradation under visible light irradiation. *ACS Sustain. Chem. Eng.* 2017, 5 (7), 5831-5841*)*.
5. Li, Y.; Gu, M.; Zhang, X.M.; Fan, J.J.; Lv, K.L.; Carabineiro, S.A.; Dong, F. 2D g-C_3N_4 for advancement of photo-generated carrier dynamics: status and challenges. *Mater. Today*, 2020, 41, 270-303.
6. Yu, X.N.; Ng, S.F.; Putri, L.K.; Tan, L.L.; Mohamed, A.R.; Ong, W.J. Point-defect engineering: leveraging imperfections in graphitic carbon nitride (g-C_3N_4) photocatalysts toward artificial photosynthesis. *Small*, 2021, 17 (48), 2006851.
7. Liu, X.L.; Ma, R.; Zhuang, L.; Hu, B.W.; Chen, J.R.; Liu, X.Y.; Wang, X.K. Recent developments of doped g-C_3N_4 photocatalysts for the degradation of organic pollutants. *Crit. Rev. Env. Sci. Tec.* 2021, 51 (8), 751-790.
8. He, F.; Wang, Z.X.; Li, Y.X.; Peng, S.Q.; Liu, B. The nonmetal modulation of composition and morphology of g-C_3N_4-based photocatalysts. *Appl. Catal. B: Environ*. 2020, 269 (15), 118828.
9. Samanta, S.; Martha, S.; Parida, K. Facile Synthesis of Au/g-C_3N_4 Nanocomposites: An inorganic/organic hybrid plasmonic photocatalyst with enhanced hydrogen gas evolution under visible-light irradiation, *Chemcatchem*, 2014, 6 (5), 1453-1462.
10. Tan, M.X.; Ma, Y.; Yu, C.Y.; Luan, Q.J.; Li, J.J.; Liu, C.B.; Dong, W.J.; Su, Y.J.; Qiao, L.J.; Gao, L.; Lu, Q.P.; Bai, Y. Boosting photocatalytic hydrogen production via interfacial engineering on 2D ultrathin Z-Scheme $ZnIn_2S_4$/g-C_3N_4 heterojunction, *Adv. Funct. Mater*. 2022, 32 (14), 2111740.
11. Deonikar,V.G.; Reddy, K.K.; Chunge, W-J.; Kim, H. Facile synthesis of Ag_3PO_4/g-C_3N_4 composites in various solvent systems with tuned morphologies and their efficient photocatalytic activity for multi-dye degradation, *J Photoch. Photobio. A Chem.* 2019, 368, 168-181.
12. Cagdas, Y.; Sule, E-E. Solar light-responsive α-Fe_2O_3/CdS/g-C_3N_4 ternary photocatalyst for photocatalytic hydrogen production and photodegradation of methylene blue, *J. Alloy Compd.* 2022, 908, 164584.
13. Shi, Y.X.; Li, L.L.; Sun, H.R.; Xu, Z.; Cai, Y.; Shi, W.L.; Guo, F.; Du, X. Engineering ultrathin oxygen-doped g-C_3N_4 nanosheet for boosted photoredox catalytic activity based on a facile thermal gas-shocking exfoliation effect. *Sep. Purif. Technol.* 2022, 292, 121038.
14. Jia, X.W.; Li, Y.F.; Liu, X.C.; Yu, X.D.; Wang, C.; Shi, Z.; Xing, Y. Highly crystalline sulfur and oxygen co-doped g-C_3N_4 nanosheets as an advanced photocatalyst for efficient hydrogen generation. *Catal. Sci. Technol.* 2022, 12(16), 5136-5142.
15. Tang, H.; Xia, Z.H.; Chen, R.; Liu, Q.Q.; Zhou, T.H. Oxygen doped g-C_3N_4 with nitrogen vacancy for enhanced photocatalytic hydrogen evolution. *Chem-Asian J.* 2020, 15(21), 3456-3461.
16. Saka, C. Surface modification with oxygen doping of g-C_3N_4 nanoparticles by carbon vacancy for efficient dehydrogenation of sodium borohydride in methanol. *Fuel*, 2022, 310, 122444.
17. Ta, X.M.C.; Daiyan, R.; Nguyen, T.K. A.; Amal, R.; Tran-Phu, T.; Tricoli, A. Alternatives to water photooxidation for photoelectrochemical solar energy conversion and green H_2 production. *Adv. Energy Mater.* 2022, 12 (42), 2201358.
18. Jia, T.K.; Fu, F.; Li, J.; Deng, Z.; Long, F.; Yu, D.S.; Cui, Q.; Wang, W.M. Rational construction of direct Z-scheme SnS/g-C_3N_4 hybrid photocatalyst for significant enhancement of visible-light photocatalytic activity. *Appl. Surf. Sci.* 2020, 499, 143941.
19. Mo, Z.; Xu, H.; Chen, Z.G.; She, X.J.; Song, Y.H.; Wu, J.J.; Yan, P.C.; Xu, L.; Lei, Y.C.; Yuan, S.Q. Self-assembled synthesis of defect-engineered graphitic carbon nitride nanotubes for efficient conversion of solar energy. *Appl. Catal. B: Environ.* 2018, 225, 154-161.
20. Wang, D.D.; Li, Y.H.; Yu, B.; Li, H.J.; Jiang, W.; Deng, X.; Wen, Y.; Liu, C.B.; Che, G.B. Improved visible-light driven photocatalysis by loading Au onto C_3N_4 nanorods for degradation of RhB and reduction of CO_2. *Adv. Powder Technol.* 2021, 32 (5), 1653-1662.
21. Li, J.H.; Shen, B.; Hong, Z.H.; Lin, B.Z.; Gao, B.F.; Chen, Y.L. A facile approach to synthesize novel oxygen-doped g-C_3N_4 with superior visible-light photoreactivity. *Chem. Commun.* 2012, 48 (98), 12017-12019.
22. Pham, X.N.; Nguyen, H.T.; Pham, T.N.; Nguyen, T.T.B.; Nguyen, M.B.; Tran, V.T.T.; Doan, H.V. Green synthesis of H-ZSM-5 zeolite-anchored O-doped g-C_3N_4 for photodegradation of Reactive Red 195 (RR 195) under solar light. *J. Taiwan Inst. Chem. E.* 2020, 114, 91-102.
23. Doan, H.V.; Nguyen, H.T.; Ting, V.P.; Guan, S.; Eloi, J.C.; Hall, S.R.; Pham, X.N. Improved photodegradation of anionic dyes using a complex graphitic carbon nitride and iron-based metal-organic framework material. *Faraday Discuss.* 2021, 231, 81-96.
24. Zhang, S.; Gu, P.C.; Ma, R.; Luo, C.T.; Wen, T.; Zhao, G.X.; Cheng, W.C.; Wang, X.K. Recent developments in fabrication and structure regulation of visible-light-driven g-C_3N_4-based photocatalysts towards water purification: a critical review. *Catal. Today*, 2019, 335, 65-77.

25. Hu, S.Z.; Ma, L.; You, J.G.; Li, F.Y.; Fan, Z.P.; Wang, F.; Liu, D.; Gui, J.Z. A simple and efficient method to prepare a phosphorus modified g-C_3N_4 visible light photocatalyst. *Rsc Adv.* 2014, 4 (41), 21657-21663.
26. Long, X.; Feng, C.; Yang, S.; Ding, D.; Feng, J.; Liu, M.; Chen, Y.; Tan, J.; Peng, X.; Shi, J. Oxygen doped graphitic carbon nitride with regulatable local electron density and band structure for improved photocatalytic degradation of bisphenol A. *Chem. Eng. J.* 2022, 435, 134835.
27. Li, K.X.; Zeng, Z.X.; Yan, L.S.; Luo, S.L.; Luo, X.B.; Huo, M.X.; Guo, Y.H. Fabrication of platinum-deposited carbon nitridenanotubes by a one-step solvothermal treatment strategy and their efficient visible-light photocatalytic activity. *Appl. Catal. B: Enviro.* 2015, 165, 428-437.
28. Cheng, C.; Zong, S.C.; Shi, J.W.; Xue, F.; Zhang, Y.Z.; Guan, X.J.; Zheng, B.T.; Deng, J.K.; Guo, L.J. Facile preparation of nanosized MoP as cocatalyst coupled with g-C_3N_4 by surface bonding state for enhanced photocatalytic hydrogen production. *Appl. Catal. B: Environ.* 2020, 265, 118620.
29. Zhang,F.; Xie, F.; Zhu, S.; Liu, J.; Zhang, J.; Mei, S.; Zhao, W. A novel photofunctional g-C_3N_4/Ag_3PO_4 bulk heterojunction for decolorization of RhB, *Chem. Eng. J.* 2013, 228,435–441.
30. Lin, X.H.; Wu, Y.; Xiang, J.; He, D.; Li, S. Elucidation of mesopore-organic molecules interactions in mesoporous TiO_2 photocatalysts to improve photocatalytic activity, *Appl. Catal. B Environ.* 2016, 199, 64–74.
31. Jiang, W.; Zong, X.; An, L.; Hua, S.; Miao, X.; Luan, S.; Wen, Y.; Tao, F.F.; Sun, Z. Consciously constructing heterojunction or direct Z-Scheme photocatalysts by regulating electron flow direction, *ACS Catal.* 2018,8, 2209–2217.
32. Zhang, J.; Xin, B.; Shan, C.; Zhang, W.M.; Dionysiou, D.D.; Pan, B.C. Roles of oxygen-containing functional groups of O-doped g-C_3N_4 in catalytic ozonation: Quantitative relationship and first-principles investigation. App. Catal. B: Environ. 2021, 292, 120155.
33. Sun, D.W.; Long, C.C.; Huang, J.H. Highly dispersed platinum-anchored g-C_3N_4 nanotubes for photocatalytic hydrogen generation. *Int. J. Hydrogen Energ.* 2023, 48(3), 943-952.
34. Wu, X.; Li, D.; Luo, B.; Chen, B.; Huang, Y.; Yu, T.; Shi, W. Molecular-level insights on NIR-driven photocatalytic H_2 generation with ultrathin porous S-doped g-C_3N_4 nanosheets. *Appl. Catal. B: Environ.* 2023, 325, 122292.
35. Wang, H.; Jiang, J.; Yu, L.; Peng, J.; Song, Z.; Xiong, Z.; Zhai, T. Tailoring advanced N-defective and S-doped g-C_3N_4 for photocatalytic H_2 evolution. *Small,* 2023, 19, 2301116.
36. Yang, B.; Han, J.; Zhang, Q.; Liao, G.; Cheng, W.; Ge, G.; Jia, X. Carbon defective g-C_3N_4 thin-wall tubes for drastic improvement of photocatalytic H_2 production. *Carbon,* 2023, 202, 348-357.
37. Wang, Y.Y.; Zhao, S.; Zhang, Y.W.; Fang, J.S.; Zhou, Y.M.; Yuan, S.H.; Zhang, C.; Chen, W.X. One-pot synthesis of K-doped g-C_3N_4 nanosheets with enhanced photocatalytic hydrogen production under visible-light irradiation. Appl. Surf. Sci. 2018, 440, 258-265.
38. Li, X.H.; Li, Y.J.; Zhu, P.F.; Jin, Z.L. Integrating Co_3O_4 with $ZnIn_2S_4$ p-n heterojunction for efficient photocatalytic hydrogen production. *Int. J. Energ. Res.* 2022, 46 (11), 15589-15601.